ORIGINAL ARTICLE

Direct numerical simulations of dense granular suspensions in laminar flow under constant and varying shear rates

Sudharsan Srinivasan[1,2,*] | **Harry E. A. Van den Akker**[1,2,3,†] | **Orest Shardt**[1,2,*]

[1]Synthesis and Solid State Pharmaceutical Centre (SSPC), University of Limerick, V94T9PX, Limerick, Ireland

[2]Bernal Institute, School of Engineering, University of Limerick, V94T9PX, Limerick, Ireland

[3]Transport Phenomena Lab, Department of Chemical Engineering, Delft University of Technology, Van der Maasweg 9, 2629 HZ Delft, The Netherlands

Correspondence
Sudharsan Srinivasan & Orest Shardt, Bernal Institute, School of Engineering, University of Limerick, Limerick, V94T9PX, Ireland
Email: Sudharsan.Srinivasan@ul.ie & Orest.Shardt@ul.ie

Present address
[†]Bernal Institute, School of Engineering, University of Limerick, Limerick, V94T9PX, Ireland

Funding information
Science Foundation Ireland (SFI)

Using an immersed boundary-lattice Boltzmann method, we investigated the response of dense granular suspensions to time-varying shear rates and flow reversals. The apparent viscosity and the evolution of particle clusters were analysed. The solids fractions and particle Reynolds numbers varied over the ranges $5\% \leq \phi_v \leq 47\%$ and $0.11 \leq Re_p \leq 0.32$. The simulations included sub-grid scale corrections for unresolved lubrication forces. The contribution of the tangential lubrication corrections to the shear stress is dominant when ϕ_v surpasses 30%. For $\phi_v > 35\%$, increasing shear-thickening is seen with increasing ϕ_v. Following a shear reversal, the number of clusters temporarily increases and then decreases to a stable value over the same time scale as the development of the wall shear stress (and apparent viscosity). Simulations with several step changes in the shear rate show the effects of the previous shear history on the viscosity of the suspension.

KEYWORDS
suspension rheology; shear reversal; time-varying shear; direct numerical simulation; immersed boundary-lattice Boltzmann method

*Corresponding authors.

1 | INTRODUCTION

Suspensions are complex fluids where the nature of the suspended particles governs their characteristics. In many areas of industry (for example, waste water treatment and slurry transport), the flow of suspensions is widely encountered inside pipelines, vessels, and pumps. The mutual interactions of particles as well as particle-fluid interactions complicate the dynamics of the flow of suspensions. A clear understanding of the rheological properties of these suspensions is necessary for the design of operations. Over the last several decades, understanding of the rheology of dense suspensions has progressed through both experimental and computational studies. Brady and Bossis (1985) used Stokesian dynamics to investigate the microstructure and the macroscopic properties (apparent viscosity: the ratio of the effective viscosity over the viscosity of the suspending fluid) of concentrated suspensions. Jogun and Zukoski (1996) conducted experiments with plate-like particles suspended inside a basic solution to study its rheological behaviour (the yielding type of response). A review article by Stickel and Powell (2005) also discusses the rheology of dense suspensions with more emphasis on microstructure and total fluid stresses. The non-Newtonian behaviour of dense suspensions, such as normal-stress differences and shear-induced migration, has been discussed by Guazzelli (2017) and co-workers (Simon et al., 2015). By coupling the lattice Boltzmann method (LBM) with a hybrid immersed boundary method (IBM) and a bounce-back scheme, Lorenz et al. (2018) demonstrated the continuous and discontinuous shear thickening of concentrated suspensions. Both Thorimbert et al. (2018) and Srinivasan et al. (2020) performed numerical simulations using LBM. The former discussed the effects of particle fraction and density ratio on the viscosity of the suspension while the latter discussed the role of particle rotation and cluster formation on the shear thickening of suspensions.

Suspension properties are well understood in dilute regimes (Bergenholtz et al., 2002; Kulkarni and Morris, 2008). However, as the solids concentration increases, the rheological characteristics of suspensions become more complex. While many researchers have reported the

steady-state rheology of suspensions (Fall et al., 2010; Dbouk et al., 2013; Brown and Jaeger, 2014), few have studied their transient behaviour. The time-dependent response of the apparent viscosity of a dense suspension may arise due to a change in the magnitude of the shear rate or a reversal of the direction of the shear flow. The first experimental observations of the response of shear stress to a reversal of the flow direction were reported by Gadala-Maria and Acrivos (1980). Experiments were performed with spherical particles in a Couette device, and they showed that for solids fractions $\phi_v > 30\%$, memory effects from the previous shearing are evident when the shear was stopped and then resumed in either the same or the opposite direction. Both Kolli et al. (2002) and Blanc et al. (2011) carried out experiments to analyse the transient response of a suspension after reversing the direction of shear flow. In recent years, interpretation of the transient rheology of suspensions through numerical simulation is gaining more attention. For example, simulations of suspensions at 45% solids submitted to shear reversal have been reported by Peters et al. (2016). More recently, Srinivasan et al. (2020) examined the history-dependent rheology of suspensions at $\phi_v = 38\%$ when subjected to a sudden increase and decrease in the shear rate.

In the present work, we analyse the time-dependent behaviour of dense suspensions (up to 47% solids by volume) via Direct Numerical Simulations (DNS). We focus on the effects of particle volume fraction and shear rate (particle Reynolds number), and in particular, we will discuss simulations of suspensions subjected to:

- a reversal of the direction of shear flow,
- increases and decreases in the shear speed in one (or more) step(s), and
- a sudden stop and then a restart of the fluid flow.

To do this, we implement an immersed boundary-lattice Boltzmann method (IB-LBM) as proposed by Feng and Michaelides (2004) in a custom C++ code (Srinivasan et al., 2020). We handle the interparticle interactions by explicitly adding lubrication force and torque correc-

tions (O'Neill and Majumdar, 1970; Nguyen and Ladd, 2002; Simeonov and Calantoni, 2012). These additional forces act over sub-grid scale distances and account for unresolved details of the flow between adjacent particles. The inclusion of these lubrication forces differentiates this study from our previous work (Srinivasan et al., 2020). We assess the contribution of these interparticle forces on the observed viscosity, comparing the simulation results with the experimental values of Krieger and Dougherty (1959) and Dbouk et al. (2013) as well as the simulations of Thorimbert et al. (2018) and Srinivasan et al. (2020).

We organise the paper in the following manner: In Sec. 2, we briefly summarise our problem statement. In Sec. 3, we briefly describe the immersed boundary-lattice Boltzmann method. Next, we discuss the implementation of lubrication corrections and show how the relative apparent viscosity of the suspension is computed from the stress on the moving walls. Finally, we show the effect of particle configurations on the viscosity of the suspension. In Sec. 4, we first present the steady-state rheology of the suspensions. Then we consider the evolution of the viscosity of dense suspensions that arises from the contribution of the resolved and unresolved (lubrication correction) stresses. Finally, we discuss the simulations mentioned in the bullet points above to investigate the nature of the transients in the evolution of suspensions in response to changes in the shear rate and its direction. We summarise our key findings in Sec. 5.

2 | PROBLEM STATEMENT

The transport of slurries through industrial pipelines motivated us to carry out the current numerical study. The dynamics of such transport is complex due to transient fluctuations in the transport rate and spatial variations along the line (in e.g., bends and valves). In this application, the solids concentration ϕ_v typically amounts to some 35%, with the flow being laminar. The carrier liquid phase is Newtonian with a kinematic viscosity ν and density ρ_f. The solid phase is assumed to consist of rigid spheres. Although our current numerical study is intended to mimic a representative volume of a suspension within a macroscopic flow, the simulation domain dimensions and boundary conditions are very similar to the parameters of a rheometer.

In a typical rheometer, a suspension of particles with radius R equal to 150 microns is contained within a 2mm gap, such that the confinement ratio $\delta = 2R/H$ (where H is the height of the simulation domain across the wall-normal z direction) amounts to 0.15. In our suspension simulations, the confinement ratio is 0.17, with $R = 4$ lu and $H = 50$ lu, where lu denotes lattice units (multiples of the simulation grid size).

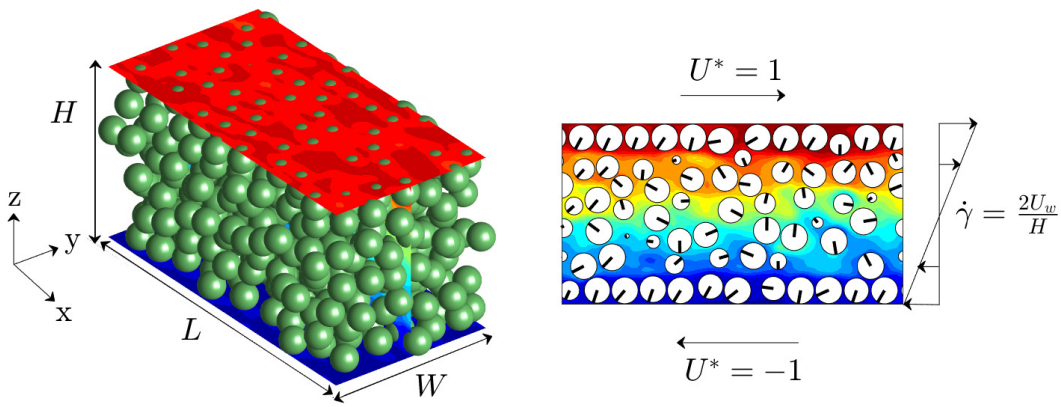

FIGURE 1 Simulation geometry with particles suspended in a Newtonian liquid subjected to simple shear flow. The left panel shows the positions of particles inside the simulation box. The right shows a 2-D visualisation of the spheres that intersect the mid-plane of the box. In both snapshots, the background colours indicate the x component of the liquid velocity scaled by the wall speed U_w.

A schematic of the simulation domain with particles suspended between two parallel plates is presented in Fig. 1. These plates move in opposite directions with a speed U_w, and we define $U^* = U_x/U_w$ (where U_x is the x component of the liquid velocity). The particles are placed randomly between the parallel walls. The flow is induced only by the shearing motion of the walls, and we do not take into account the effects of gravity. The imposed shear rate is $\dot{\gamma} = 2U_w/H$. The simulation box is periodic in the shear (x) and vorticity (y) directions. We determine the relative apparent viscosity of the suspension under steady-state and transient conditions by varying the wall speed (shear rate) and the number of particles (solids volume fraction).

3 | SIMULATION METHODS

3.1 | The immersed boundary-lattice Boltzmann method

We solve the flow of the interstitial Newtonian liquid with a common lattice Boltzmann technique (Chen and Doolen, 1998). We used a $D3Q19$ model (19 discrete velocities in 3-D), the usual BGK collision operator, and the Shan and Chen (1993) forcing scheme for incorporating a body force (which is used by the immersed boundary method to account for the presence of solid particles). The wall speed in the simulation was kept well below the speed of sound to simulate an incompressible flow. An explicit leapfrog integration scheme was used to solve the translational and angular motion of the particles. For more details, the reader is referred to our earlier paper (Srinivasan et al., 2020). We have previously tested the accuracy of the implemented IB-LBM code by evaluating the translation of a single rigid sphere at a constant speed in Newtonian liquid (Srinivasan et al., 2020). In a simulation with a sphere of radius $R = 4$ lu, the effective size of the sphere (its hydrodynamic radius R_{hyd}) increased by about 5% (4.2 lu) in comparison with the input radius R. Therefore, in the sections that follow, we use this calibrated radius to compute the solids volume fraction as well as the particle Reynolds number $Re_p = \dot{\gamma} R_{hyd}^2 / \nu$.

3.2 | Lubrication corrections

The main difference between the suspension simulations described in this paper and our previous study (Srinivasan et al., 2020) is that we now consider higher solids volume fractions and include corrections for unresolved lubrication forces and torques between particles. When the distance between the surfaces of two spheres (or between a sphere and a wall) approaches the resolution of the simulation grid, the simulation can no longer resolve the flow of liquid in the gap. Therefore, explicit lubrication force and torque corrections (both normal and tangential) are included to account for the unresolved flow. The expression for the leading order normal lubrication force correction on the particle p due to relative translation of the spheres p and q along the line connecting the centres of the spheres is given by (Ten Cate et al., 2004; Simeonov

and Calantoni, 2012)

$$\mathbf{F}_p^{n,lub} = 6\pi\mu R_{hyd}\frac{\alpha^2}{(1+\alpha)^2}\left(\frac{1}{h}-\frac{1}{h_o^n}\right)(\mathbf{U}_{pq}\cdot\mathbf{n}_{pq})\mathbf{n}_{pq}. \quad (1)$$

The superscript n denotes normal. For a monodisperse suspension, the ratio of the radii of spheres p and q is $\alpha = R_{hyd}^q/R_{hyd}^p = 1$, while $h = |\mathbf{x}_q - \mathbf{x}_p| - 2R_{hyd}$ is the gap between particles, where $\mathbf{x}_p$ and $\mathbf{x}_q$ are the centres of spheres p and q respectively. $\mathbf{U}_{pq} = \mathbf{u}_q - \mathbf{u}_p$ is the relative translational speed, and $\mathbf{n}_{pq}$ is the unit vector that points from the centre of sphere p to the centre of sphere q. h_o^n is the cutoff gap below which the normal lubrication correction is applied. The lubrication forces do not saturate at small gap sizes, and additional repulsive force is not included in the simulations to prevent overlap - for the cases we consider, the divergence of the lubrication (correction) force with decreasing gap size is sufficient to prevent overlap. The value $h_o^n/R_{hyd} = 0.72$ is chosen by performing a simulation of the head-on collision of two spheres with $R = 4$ lu, and it ensures that the force on the spheres is correct in the limit of small gaps. Several similar benchmark simulations have been conducted to determine the cutoffs for the tangential lubrication force and torque corrections. The details of the equations used for implementing the tangential lubrication correction as well as their corresponding cutoff values are given in Appendix A.

The integration of particle motion uses smaller timesteps than the LBM flow solver. We ensure stability of the explicit scheme for integration of the particles' motion by using n_{tp} equal sub-timesteps for every fluid timestep. For $\phi_v \leq 40\%$, a constant number of sub-timesteps was used throughout each simulation, and the required value of n_{tp} that is needed to ensure stability increases with increasing ϕ_v and Re_p. To assess the effect of the number of sub-timestpes, we considered simulations at $\phi_v = 17\%$ and 25% with $Re_p = 0.32$. For $\phi_v = 17\%$, the difference in the apparent viscosity was 0.02% when increasing the number of sub-timesteps from 50 to 100. The difference was 0.14% at $\phi_v = 25\%$ when using 70 and 150 sub-timesteps. The viscosities are therefore not sensitive to the number of sub-timesteps. For $\phi_v = 47\%$, we used an adaptive time-stepping scheme. Whenever overlap between two particles or between a particle and wall

is detected, the number of sub-timesteps is doubled until overlap does not occur. If overlap is not detected, the number of sub-timesteps is halved. The typical number of sub-timesteps in these simulations was 512.

The computation of interparticle interaction forces is accelerated by the use of a binning algorithm instead of checking all pairs of particles to find those that are sufficiently close to applying lubrication corrections. The simulation domain is divided into a grid, and all particles are assigned to a cell within the grid. The algorithm then compares only the positions of particles that are in adjacent cells. With this algorithm, the suspension simulations were approximately seven times faster than with the less-efficient alternative.

3.3 | Relative apparent viscosity

The relative apparent viscosity η_r of the suspension is determined as the sum of the resolved fluid shear stress and the lubrication correction for particle-wall interactions. First, we evaluate the local fluid shear stress on every lattice node adjacent to the sheared walls (top and bottom) as

$$\tau_w^{LB} = \mu \frac{U_x - U_w}{\Delta y} \tag{2}$$

where $\Delta y = 0.5$ lu is the distance between the wall and the neighbouring fluid node. The superscript LB denotes the fluid contribution to the shear stress on either wall w. These local shear stresses are averaged across the $x - y$ cross-sectional plane to obtain the total fluid shear stress. In the simulations with tangential lubrication force and torque corrections, the additional stress $\tau_w^{lub} = \dfrac{\frac{1}{LW}\sum F_w^{lub}}{\mu\dot{\gamma}}$ (with F_w^{lub} being the force on particles that arise from the contact with solid walls) due to translation and rotation of any particle near either wall is added to Eq. 2. The overall stress of the suspension on the walls, and therefore, the relative apparent viscosity is obtained as

$$\eta_r = \frac{\langle \tau_w^{LB} \rangle + \tau_w^{lub}}{\mu\dot{\gamma}}. \tag{3}$$

In this equation, $\langle\ \rangle$ denotes the average over the $x-y$ cross-sectional area. The apparent viscosity may be computed from the stresses on either of the two walls. In the discussion that follows, the average of the apparent viscosities calculated from the stresses on the top and bottom walls is used: $\bar{\eta}_r = (\eta_r^t + \eta_r^b)/2$.

4 | THREE-DIMENSIONAL SIMULATIONS OF SUSPENSIONS

Three-dimensional simulations of dense monodisperse suspensions have been performed in simple shear flow. In these simulations, the solids fraction ϕ_v was varied between 5% and 47% and the particle Reynolds number between 0.11 and 0.32. The suspensions are neutrally buoyant (ratio of the particle and fluid densities is $\sigma = \rho_p/\rho_f = 1$). The liquid kinematic viscosity is $\nu = 1/30$ lu^2/ts. Explicit lubrication corrections (normal and tangential), as previously described, were included to account for sub-grid scale details of the flow between solid surfaces. Simulations of dense suspensions (that is, $\phi_v \geq 25\%$) ran on ICHEC (Irish Centre for High End Computing) machines with 2×20 core 2.4 GHz Intel Xeon Gold 6148 (Skylake) processors with 192 GB RAM. Local computing resources with 4 core Intel i7-6700 processor of 64 GB RAM was used to simulated dilute suspensions ($\phi_v < 25\%$).

4.1 | Particle initialisation

Several different approaches were taken to specify the initial positions of the spheres over the range of solids volume fractions that we consider in this study. For suspensions up to 38% solids, random initialisation of the positions was implemented, and we discuss the rheology of suspensions with two such random initial states. By random packing of non-overlapping spheres (inside the simulation domain as well as across the periodic boundaries), we were able to achieve up to a maximum of 35% solids (that is, $N_p = 280$, where N_p is the number of particles). To reach 38% solids by volume ($N_p = 310$), we used the same random initialisation except for that overlap across the periodic boundaries was accepted. Then, we applied a spring-like repulsive force (Srinivasan et al., 2020) to separate any contact.

At $\phi_v = 40\%$, we used a regular cubic packing and considered two different configurations as presented in Fig. 2. In the first configuration (set a), we stacked the spheres with a gap of

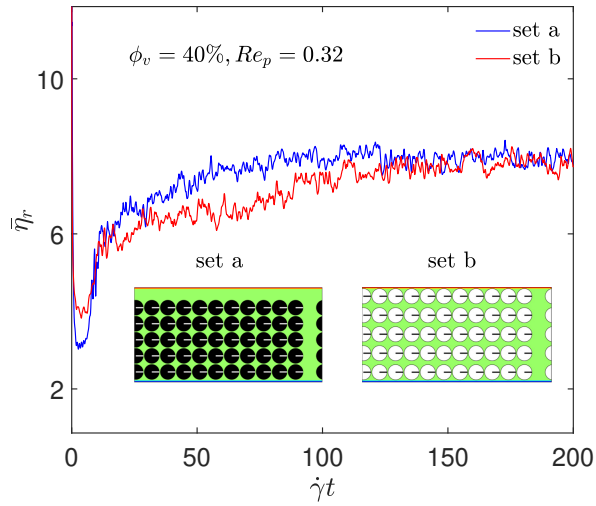

FIGURE 2 Differences in the evolution of the relative apparent viscosity of a suspension as a function of dimensionless time for two different initial particle configurations (set *a* and set *b*). For this example, $\phi_v = 40\%$ and $Re_p = 0.32$, and only normal lubrication corrections were included. The insets show the two initial conditions.

0.4 lu which left additional gaps near $x = L$, $y = W$, and $z = H$ (7 lu, 1.5 lu, and 6.67 lu, respectively). In the second case (set b), we retained the large gap near the periodic boundaries ($x = L$ and $y = W$) and stretched the gaps along the wall-normal z direction while maintaining a gap of 0.5 lu between the particles and the top and bottom plates. The inset in Fig. 2 shows cross-sections through the two initial particle configurations. Both suspensions started from rest and were sheared until steady-state (that is, until we observed steady fluctuations in the average viscosity). While both suspensions attain approximately the same viscosity in the long run (the difference is $\approx 4\%$), the evolution of the viscosity towards this equilibrium depends on the initial particle configuration. Finally, to achieve $\phi_v = 47\%$, we specified the initial positions of 432 spheres by using a cubic packing with small random displacements.

For simulations up to 38% solids, the simulation domain was $100 \times 50 \times 50$ lu. To achieve more dense suspensions, we slightly altered the domain size by increasing the dimension along the streamwise (x), spanwise (y), and wall-normal (z) directions to 100 lu, 52 lu, and 50 lu for 40% solids, and 102 lu, 52 lu, and 54 lu for 47% solids, respectively. A grid independence

study has been previously reported (Srinivasan et al., 2020), and our results are not sensitive to increases in domain size along the periodic boundaries as well as across the channel height. Therefore, a domain size of $100 \times 50 \times 50$ lu with particles of $R = 4$ lu is sufficient to represent larger domains.

4.2 | Steady-state rheology

In Fig. 3, we present the average relative apparent viscosity of suspensions computed using only normal lubrication corrections and the combination of both normal and tangential lubrication corrections. In all these simulations, the suspension was sheared up to a strain of $\dot{\gamma}t = 200$. The presented results are time averaged (over $100 \leq \dot{\gamma}t \leq 200$) and compared with Krieger and Dougherty (1959) with the parameters $B = 2.5$ and $\phi^c = 0.60$, Dbouk et al. (2013), and simulations of Thorimbert et al. (2018) at $Re_p = 0.1$ and $\sigma = 1.3$ and Srinivasan et al. (2020) at $Re_p = 0.11$, 0.33, and 0.55 and $\sigma = 1$.

Fig. 3 shows how the relative apparent viscosity of the suspension increases with an increase in solids concentration. For dilute suspensions (that is, $\phi_v = 6\%$ and 12%), our viscosities agree with Krieger and Dougherty (1959). Up to $\phi_v = 25\%$, the viscosities computed by the spring force simulations of Thorimbert et al. (2018) and Srinivasan et al. (2020) are in good agreement with the present results. It is also evident that in this dilute regime the particle Reynolds number does not affect the viscosity of the suspension. As the solids fraction increases ($\phi_v \geq 30\%$), we see that the computed viscosities diverge from the data reported by Thorimbert et al. (2018) and Krieger and Dougherty (1959) and approach the values of Dbouk et al. (2013). In the simulations with only the normal lubrication correction (filled green symbols), we can see that the effect of Re_p becomes noticeable for $\phi_v \geq 30\%$ and the suspension exhibits shear-thickening (when ϕ_v exceeds 35%). Interestingly, from the simulations with both normal and tangential lubrication corrections (filled orange symbols), we observe a transition from weak shear-thinning (at 30% and 35% solids) to shear-thickening ($\phi_v \geq 40\%$). A similar transition in the rheological behaviour was also observed in the transient simulations – details are given in the upcoming section. Over the range of solids concentrations presented (that is from 2% to

47% solids), we can see that the viscosities computed using simulations with both normal and tangential lubrication corrections are in good agreement with the experiments of Dbouk et al. (2013).

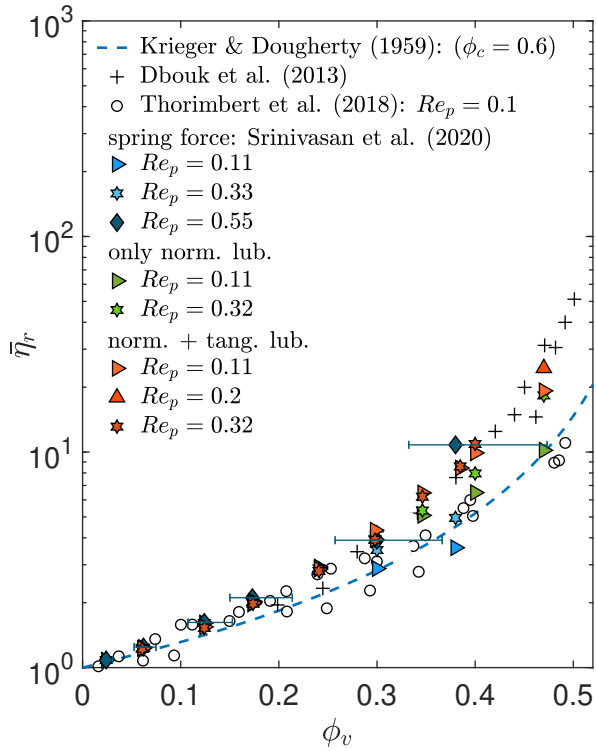

FIGURE 3 Comparison of the computed average apparent viscosities $\bar{\eta}_r$ (filled symbols) for varying solids volume fraction and Re_p with Krieger and Dougherty (1959) (dashed line), Dbouk et al. (2013) (pluses), Thorimbert et al. (2018) (open circles), and Srinivasan et al. (2020) (filled symbols in different shades of blue). While the left and right error bars show the solids volume fraction computed using $R_{input} = 4$ lu and $R_{spring} = 4.5$ lu, the symbol is at ϕ_v calculated with $R_{hyd} = 4.2$ lu.

At 47% solids, we were able to simulate suspensions up to $Re_p = 0.2$ with the current numerical scheme before encountering instability in the integration of particle motion. Horizontal error bars are presented for the simulations from our previous study (Srinivasan et al., 2020) at $Re_p = 0.55$ to show the range of ϕ_v for different estimates of the particle radius. In these previous simulations, a repulsive force is applied when $h < 1$ lu to separate particles. In Fig. 3, the symbol is drawn at the volume fraction that corresponds to the hydrodynamic radius

$R_{hyd} = 4.2$ lu. The error bars to the left and right correspond to ϕ_v calculated based on the input radius $R_{input} = 4$ lu (which is the radius of the sphere on which the tracking points of the immersed boundary method are located) and the spring radius $R_{spring} = 4.5$ lu (which follows from the separation distance imposed by the repulsive spring force). Interestingly, we see that the results match the Krieger and Dougherty (1959) correlation if ϕ_v was computed based on the spring radius. In the current simulations, this effect is no longer present.

4.3 | Transient rheology

In the steady-state rheology calculations, the shear rate was constant throughout the simulation. In many scenarios, the direction and rate of shear may vary in time and space. Therefore, it is also interesting to learn about how the structure and rheology of suspensions responds to changes in the shear rate.

Before going into the details of simulations with time-varying shear, we first consider in Fig. 4 the transient evolution of the apparent viscosity of a suspension under constant shear. This figure shows the contributions of the resolved (LBM) and unresolved (explicit lubrication correction) stresses. The solids volume fractions were $\phi_v = 6\%, 30\%, 38\%$ and 47%, and $Re_p = 0.11$. At $\phi_v = 47\%$, the resolved fluid stress (see Eq. 2) first increases up to $\dot{\gamma}t \approx 5$ and then decreases before it start to stabilise after $\dot{\gamma}t \approx 10$. Contrarily, the lubrication stresses are negligible until $\dot{\gamma}t \approx 5$ due to the initial gap between the particles and the top and bottom walls. As the suspension is sheared, some particles approach to within the cutoff distance from the walls, and the lubrication stress increases rapidly up to $\dot{\gamma}t \approx 20$ and then stabilise. The smaller figures along the top of Fig. 4 present the evolution of the stresses for several lower volume fractions. For dilute suspensions, lubrication stresses are negligible compared with the resolved fluid stresses (that is, Eq. 2). As the suspension becomes denser, the number of particles adjacent to a wall increases (see the 2-D cross-sections along the bottom of Fig. 4), and therefore, the lubrication corrections overtake the resolved fluid stress. Lubrication and resolved stresses are comparable in magnitude when the solids volume fraction is 30%.

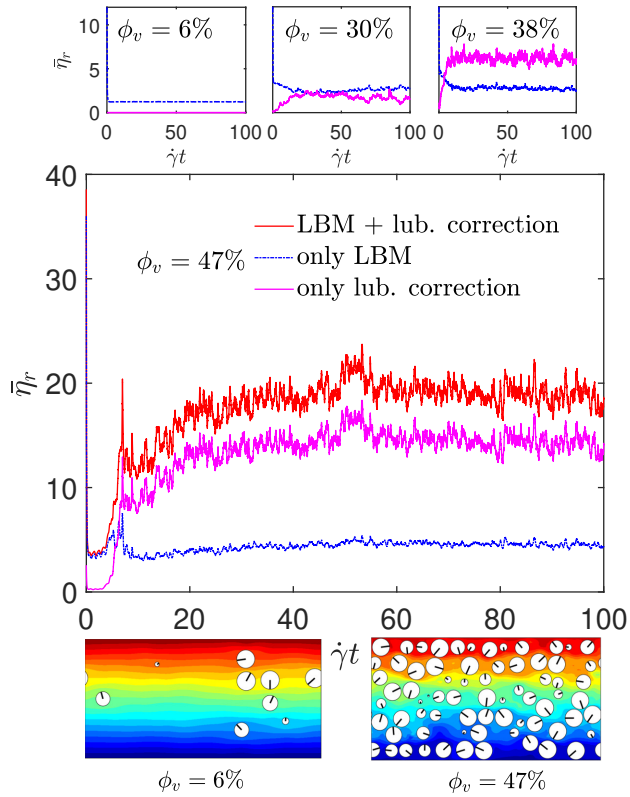

FIGURE 4 Contributions of resolved (dashed blue lines, 'only LBM') and unresolved shear stresses (solid magenta lines, 'only lub. correction') to the relative apparent viscosity (solid red lines, 'LBM + lub. correction') of a suspension as a function of dimensionless time ($\dot{\gamma}t$) at $\phi_v = 47\%$ and $Re_p = 0.11$. Figures along the top show the trends for $\phi_v = 6\%$, 30%, and 38%. Images along the bottom show cross-sections through the simulation domains $\phi_v = 6\%$ (left) and 47% (right) at $\dot{\gamma}t = 50$.

4.3.1 | Effects of shear reversal

We now discuss the transient behaviour of suspensions subjected to changes in the direction of the shear while keeping the rate constant. For several values of ϕ_v varying between 10 and 40% and particle Reynolds numbers $Re_p = 0.11$ and 0.32, we present in Fig. 5 the numerical results of shear reversal simulations. The apparent suspension viscosity is plotted as a function of the accumulated strain after the time of the reversal (t^r). In all these simulations, the suspension was first sheared up to $\dot{\gamma}t^r = 30$ (except at $\phi_v = 40\%$, where $\dot{\gamma}t^r = 40$ to ensure steady fluctuations) in one direction. After reversing the shear flow ($t \geq t^r$), all simulations ran to the same strain ($\dot{\gamma}(t - t^r) = 30$). Consistent with our observation from the constant shear simulations (Fig. 3), even after flow reversal, we can see that the rheology of the suspension changes from weak shear-thinning (at 30% and 33% solids) to weak shear-thickening (at $\phi_v \geq 40\%$).

We relate these transitions in the rheological behaviour of suspensions to the rotation rates of particles (Srinivasan et al., 2020). In dilute suspensions, the particles rotate at half the imposed shear rate (that is, $\omega_p = \dot{\gamma}/2$); however, as the solids concentration increases, clustering of particles increases. As a result, several groups of particles revolve together at a slower rate. Overall, the rotation of clusters has a significant effect on the transport of momentum and therefore, the relative viscosity (Srinivasan et al., 2020).

At $t = t^r$, the shear stress on the walls (and thus the computed apparent viscosity of the suspension) increases suddenly from its previous value and then decreases. For low solids volume fractions (10% and 17%), the viscosity continues to decrease until reaching the previous steady value. With increasing solids concentration ($\phi_v \geq 30\%$), the viscosity first decreases below its previous steady value and then increases. The magnitude of the temporary decrease in the viscosity increases with increasing solids fraction. The insets in the figures on the right of Fig. 5 present a comparison of the simulated viscosities ($Re_p = 0.11$) with the experimental values of Blanc et al. (2011) ($Re_p \sim 10^{-9} - 10^{-7} \ll 1$). At 30% solids, the minimum viscosity after shear reversal and the steady value are consistent with Blanc et al. (2011). At the higher volume fraction (40% solids), the minimum simulation viscosity deviates from Blanc et al.

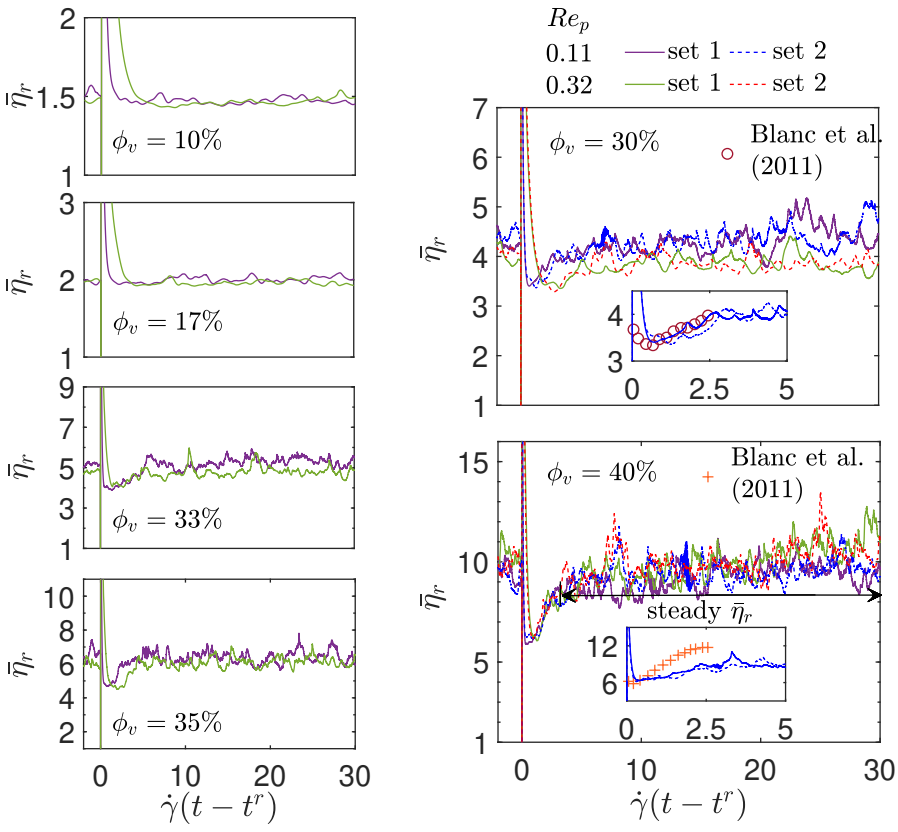

FIGURE 5 Average relative apparent viscosity $\bar{\eta}_r$ as a function of accumulated strain after reversal in the shear direction for $Re_p = 0.11$ (purple lines) and 0.32 (green lines). The solids concentration varies from 10% to 40%. Insets in the figures on the right show a comparison of the numerical results (solid lines) obtained by IB-LBM for $\phi_v = 30\%$ and 40%, and $Re_p = 0.11$ with the experimental results (symbols) of Blanc et al. (2011) under Stokes condition ($Re_p \sim 10^{-9} - 10^{-7}$). Computations for an additional random initial condition (dashed lines) are shown for $\phi_v = 30$ and 40%.

(2011) by ≈ 4%. From a steady value of about 10 prior to the flow reversal, the viscosity in this simulation drops to a minimum of ≈ 7. Though the steady structure of the particle arrangement is destroyed temporarily due to reversal of the flow direction, the structure eventually rebuilds and the relative viscosity returns to 10 (average over $10 \leq \dot{\gamma}(t - t^r) \leq 30$). Simulations with a different random initial particle configuration (set 2) for 30 and 40% solids at $Re_p = 0.11$ and 0.32 show that the details of the fluctuations are different but the general trends remain the same. For set 2, $\bar{\eta}_r$ is higher than for set 1 by ≈ 2% for both Reynolds numbers and solids volume fractions.

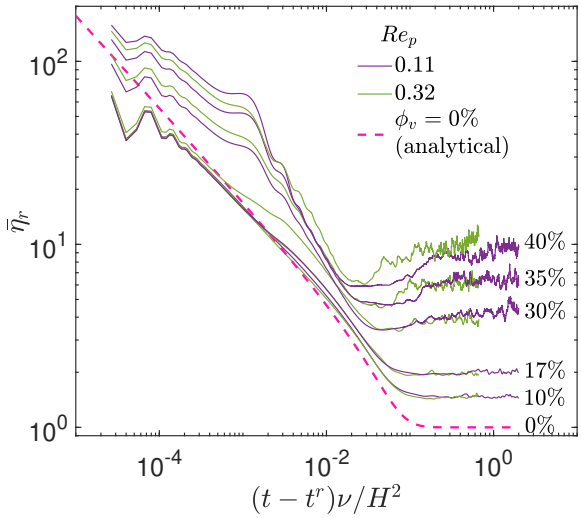

FIGURE 6 Wall shear stress (expressed as the implied average relative apparent viscosity $\bar{\eta}_r$) after shear reversal as a function of time scaled by the viscous time scale H^2/ν. The solids volume fractions vary from 0% to 40% in the order of increasing viscosity, and $Re_p = 0.11$ and 0.32. The initial particle positions correspond to set 1 of Fig. 5. The dashed magenta line shows the analytical solution for the stress in the absence of suspended particles ($\phi_v = 0\%$).

With an increase in the solids concentration, we observe a delay in the development of the suspension viscosity that decreases with increasing ϕ_v. We analyse the reason for this delay by considering the development of the viscosity of the suspension over two time scales. The first of these scales is the viscous time scale based on the domain height, and the second is an advection time scale based on the mean free path between particles. Fig. 6 presents a comparison of the

average apparent viscosity as a function of $(t-t^r)\nu/H^2$ for ϕ_v between 10% and 40% and Re_p = 0.11 and 0.32. We can see that the minimum viscosities coincide for both Re_p, which indicates that the dynamics of the first stage (the attainment of the minimum viscosity) are determined by the viscous time scale. For 10% and 17% solids, the initial decreases in the viscosity of the suspension have similar slopes until becoming steady for $(t-t^r)\nu/H^2 \geq 0.1$. With increasing solids, the slope of $\bar{\eta}_r$ increases, and the time to reach the minimum viscosity decreases (relative to the viscous time scale) as the higher amount of solids increases the apparent viscosity (and accelerates momentum transport). In Fig. 6, we also present the analytical solution (Bird et al., 2007) for the developing shear stress in the absence of particles (dashed magenta line). The slope from the LB simulation with $\phi_v = 10\%$ matches the analytical solution well during the initial development of the wall shear stress. Under the steady-state condition, the analytical relative apparent viscosity must be exactly equal to 1. The deviation of $\bar{\eta}_r$ in the simulation for $(t-t^r)\nu/H^2 > 0.1$ reflects the higher viscosity of a suspension with 10% solids.

Re-structuring of the suspension occurs over an advective timescale. Taking $\dot{\gamma}R_{hyd}$ as the velocity scale and the mean free path $l = \sqrt[3]{V/N_p} = R_{hyd}\sqrt[3]{4\pi/(3\phi_v)}$ (where V is the volume of the simulation domain) as the length scale, we form the advective time scale $l/(\dot{\gamma}R_{hyd})$. Fig. 7 shows the development of $\bar{\eta}_r$ as a function of time scaled by this advective time scale starting from rest with a random particle configuration (left panel) and after a reversal of the shear direction (right panel). For this analysis, we consider solids volume fractions up to 47% and $Re_p = 0.11$. For the development from rest in a random configuration, the differences in the initial trends at higher concentrations (ϕ_v = 40 and 47%) are due to the use of a cubic packing. The right panel of Fig. 7 shows that the apparent viscosity evolves differently after a reversal. In all cases (both from rest and after reversal), a steady viscosity is achieved after $\approx 3l/(\dot{\gamma}R_{hyd})$ for concentrated suspensions ($\phi_v \geq 30\%$). As the solids concentration increases, the mean free path decreases, and the suspension requires less time to attain a stable configuration. As shown on the right of Fig. 7, the non-dimensional time to reach steady fluctuations is the same at a higher Reynolds number ($Re_p = 0.2$) for $\phi_v = 47\%$.

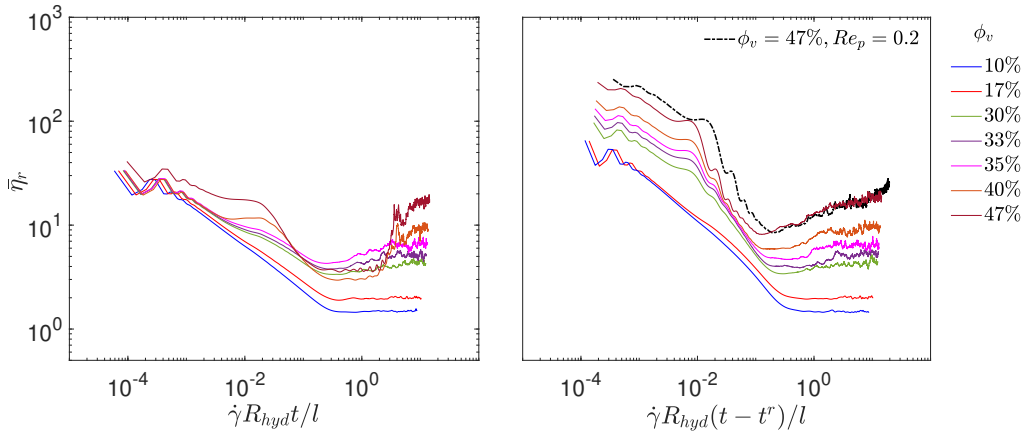

FIGURE 7 Development of the average relative apparent viscosity of suspensions starting from rest with random particle positions (left) and after reversal of the shear direction (right). Time is scaled by the advective time scale $l/(\dot{\gamma}R_{hyd})$, with the mean free path l defined in the text. For all solids concentrations ($10\% \leq \phi_v \leq 47\%$) the particle Reynolds number is 0.11. Additional data for $\phi_v = 47\%$ with $Re_p = 0.2$ is also shown on the right (dashed black line).

Analysis of the evolution of the number of clusters in the simulations of shear reversal shows that the average cluster size increases with increasing solids concentration. Presented in Fig. 8 is a comparison of the evolution of the number of clusters as a function of time for several solids concentrations. A cluster is defined as a collection of two or more particles in which the gap between each particle and at least one other particle in the cluster is smaller than a cutoff distance h_c. In dilute suspensions (for instance, $\phi_v = 10\%$) there is a limited number of particles, and therefore the likelihood of clusters forming is low. In dense suspensions (for example 47% solids), the particles are closely packed and have a greater tendency to form several small clusters or one cluster with several particles. To demonstrate changes in the evolution of particle clusters, h_c was chosen to obtain approximately 20 clusters at steady-state for each solids concentration. In concentrated suspensions ($\phi_v > 30\%$), a temporary rise in the number of clusters is seen after a reversal of the shear direction. It is interesting to see that the peaks are similar with a maximum of approximately 50 clusters for all such dense suspensions. The bottom right corner of Fig. 8 shows the dependence of the average cluster number after flow reversal on the choice of the threshold for several concentrations. The average cluster number

is computed as $\bar{N}_p^c = N_p N_s / N_c^t$, where N_c^t is the total number of clusters (including all single particles) counted over N_s equally-spaced samples of the simulation state. With an increase of ϕ_v, it is evident that the average cluster number increases. While for 10% solids, the average cluster number is approximately 1.2 at $h_c/R_{hyd} = 0.119$, for the same cluster threshold $\bar{N}_p^c$ at 47% solids is 244.5. For dense suspensions, small changes in the cluster threshold lead to large differences in the number of clusters.

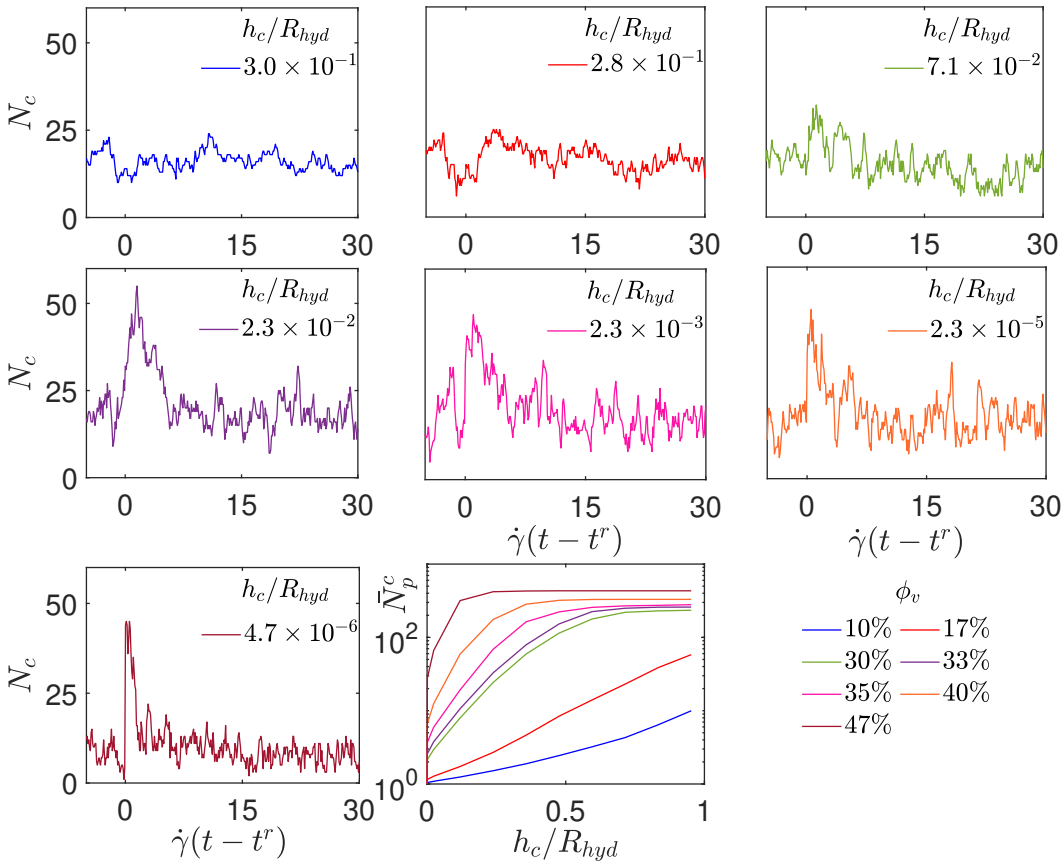

FIGURE 8 Evolution of the number of clusters N_c as a function of non-dimensional time $\dot{\gamma}(t - t^r)$ after a reversal of the shear direction for several solids fractions and cluster cutoffs at $Re_p = 0.11$. In all simulations, the cluster threshold h_c/R_{hyd} was chosen to yield ≈ 20 clusters at steady state. At $\dot{\gamma}(t - t^r) = 0$, sudden peaks for $\phi_v \geq 30\%$ indicate the switch in flow direction. The dependence of the average cluster size $\bar{N}_p^c$ on the cutoff distance h_c/R_{hyd} is shown in the bottom right corner.

4.3.2 | Effects of step-changes in the shear rate

We now study the transient behaviour of dense suspensions in response to step-changes in the magnitude of the shear rate. For this purpose, we consider two solids fractions, $\phi_v = 40\%$ and 47%. At 40% solids, we used the same initial cubic packing as previously (sets 1 and 2 in Fig. 2). To show trends more clearly, $\bar{\eta}_r$ is obtained by averaging the results for the two initial particle arrangements. For 47% we use an initial particle configuration from the period of steady fluctuations shown in Fig. 4. The number of sub-timesteps is constant for 40% solids, and it is determined by the requirements for the highest Re_p to ensure stability throughout the simulations. The adaptive algorithm for the number of sub-timesteps was used for 47% solids.

The left-hand panel of Fig. 9 shows the evolution of the average relative apparent viscosity as a function of the accumulated strain $\dot{\gamma}_o t$ starting from rest ($\dot{\gamma}_o$ is the shear rate that corresponds to $Re_p = 0.1$). The shear rate is increased in two different ways: a single step up to $Re_p = 0.2$ (red lines) at $\dot{\gamma}_o t = 18.5$ and in two steps (blue lines) – an intermediate step to $Re_p = 0.15$ at $\dot{\gamma}_o t = 12.7$ and then another step to $Re_p = 0.2$ at $\dot{\gamma}_o t = 18.5$. The shear rate then remains steady until $\dot{\gamma}_o t = 24.2$. For comparison, we also show the data for simulations with a constant shear rate ($Re_p = 0.1$; green lines). Considering the range of the fluctuations, we conclude that the apparent viscosities after shearing at $Re_p = 0.2$ are the same as with $Re_p = 0.1$ for both solids fractions. The result is the same whether the shear rate is increased in a single step or two steps; the average relative viscosities are 10 ($\phi_v = 40\%$) and 17 ($\phi_v = 47\%$).

After shearing the suspensions at $Re_p = 0.2$, we consider how the viscosity of the suspensions develops when the shear rate is returned to $Re_p = 0.1$ (right panel of Fig. 9). At the lower solids fraction (40%), the relative viscosity shows no significant history effect, returning to ≈ 10 for all cases. For $\phi_v = 47\%$, however, temporary shear at a higher speed results in an increase in the apparent viscosity when the shear rate returns to its previous value. In the simulations with one and two step increases, the viscosity increases by 35% to 23. Considering the range of the fluctuations, it is not clear whether there is a difference between a single step increase or multiple increases with a smaller magnitude. The right panel of Fig. 9 includes

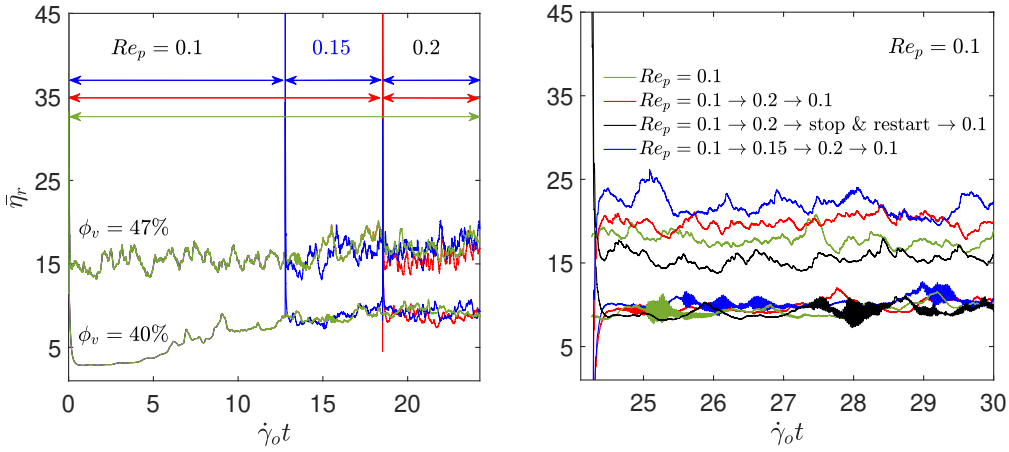

FIGURE 9 Average relative apparent viscosity as a function of time for suspensions with $\phi_v = 40\%$ (bottom set; lower viscosity) and 47% (top set; higher viscosity). In the left panel, the coloured arrows at the top show the durations of the different shear rates for each case. The right panel shows the evolution of average viscosity after bringing the shear rate back to its original value (that is, $Re_p = 0.1$) from the previous high shear regime. The black line in the right panel shows the result of stopping the fluid and particle motion at $\dot{\gamma}_o t = 24.2$ and restarting from the particle positions at that time.

one additional case (black lines): instead of continuing from the complete simulation state of the red case at the end of shearing at $Re_p = 0.2$, the fluid and particle velocities are reset to zero. The only history that is retained is the positions of the particles but not their speeds or the motion of the interstitial fluid. The apparent viscosities in these cases are effectively the same as those for constant shear: within 2% at $\phi_v = 40\%$ and 6% at $\phi_v = 47\%$. Therefore, restarting the flow cancels out the effects of temporary shear at a higher rate. From these observations, we conclude that the rheology of suspensions depends not only on the positions of the particles (the microstructure of the suspension) but also the fluid history.

5 | CONCLUSIONS

Three-dimensional direct numerical simulations of suspensions have been performed using an immersed boundary-lattice Boltzmann method for Reynolds numbers in the range $0.1 \leq Re_p \leq 0.3$ and solids volume fractions from 5% to 47%. The simulations included corrections for unresolved lubrication forces and torques over sub-grid scale distances. Up to $\phi_v = 47\%$ solids, the relative apparent viscosity of suspensions computed from the simulations with normal and

tangential lubrication corrections showed good agreement with the experimental data due to Dbouk et al. (2013) but deviate from the correlation data of Krieger and Dougherty (1959) and simulations of Thorimbert et al. (2018). The viscosity of the suspension showed no dependence on the Reynolds number for $\phi_v \leq 17\%$, weak shear-thinning at $\phi_v = 30$ and 35%, and shear-thickening for $\phi_v \geq 40\%$. As the solids concentration increases ($\phi_v \geq 30\%$), the unresolved stress due to translation and rotation of particles near the walls contribute substantially to the total stress on the walls and therefore the apparent viscosity.

Simulations of suspensions submitted to shear reversal have been performed for solids fractions between 10 and 47% with $Re_p = 0.11$ and 0.32; for 47% solids, simulations were run for $Re_p = 0.1$ and 0.2. The initial development of the shear stress after a reversal follows a viscous time scale. Dilute suspensions ($\phi_v \leq 17\%$) follow the trend of a pure Newtonian fluid ($\phi_v = 0\%$). At higher volume fractions, a minimum shear stress is observed before the shear stress rises to a steady value that depends on the imposed shear rate. This minimum stress is the same for both Re_p. As ϕ_v increases, the mean free path decreases and therefore, the suspension requires less time to re-structure and attain a stable assembly. An advective timescale based on this mean free path governs the dynamics of the re-structuring of the suspension towards a steady apparent viscosity.

Over this advective time scale, evolution in the number of clusters is also evident in dense suspensions ($\phi_v \geq 30\%$). For ϕ_v between 10 and 47%, the time-evolution of the microstructure is demonstrated by choosing an appropriate cluster threshold. After reversing the flow direction, the structure of the particle assembly collapses, and a temporary increase in the number of clusters is seen. The previous structure then rebuilds to form a stable cluster configuration. At the highest solids fraction we considered (47% solids), simulations with step increases in the magnitude (but not the direction) of the shear rate showed a 35% higher viscosity when the shear rate was returned to its initial value. At low fractions ($\phi_v = 40\%$), history effects on the viscosity of the suspension were negligible. The memory effect seen at $\phi_v = 47\%$ was removed by stopping the motion of the fluid and particles before shearing again at the initial rate.

Our next aim is to examine the effects of including surface potentials on the steady-state and transient rheology of dense suspensions. For this purpose, we will study the effects of electrostatic repulsion and Van der Waals attraction forces as a function of the particle Reynolds number and solids volume fraction.

ACKNOWLEDGMENTS

O.S. thanks Azam Karimimamaghan for assistance with the implementation of the binning algorithm for identifying pairs of particles within a specified distance of each other. This research was conducted with the financial support of the Synthesis and Solid State Pharmaceutical Centre (SSPC), funded by the Science Foundation Ireland (SFI) and co-funded by the European Regional Development Fund under Grant Number 14/SP/2750. We thank the Irish Centre for High-End Computing (ICHEC) for the provision of computational facilities and support.

APPENDIX A

In this appendix, we list the equations for computing the tangential lubrication force and torque corrections. First, the tangential lubrication force on the p^{th} particle due to translation and rotation of the spheres perpendicular to the centerline is (O'Neill and Majumdar, 1970; Simeonov and Calantoni, 2012)

$$\begin{aligned}\mathbf{F}_p^{t,lub} &= 6\pi\mu R_{hyd}\left[\frac{4\alpha(2+\alpha+2\alpha^2)}{15(1+\alpha)^3}\ln\left(\frac{h}{h_o^t}\right)+O(1)\right]\mathbf{U}_t\\ \mathbf{F}_p^{r,lub} &= 6\pi\mu R_{hyd}^2\left[\frac{2\alpha^2}{15(1+\alpha)^2}\ln\left(\frac{h}{h_o^r}\right)+O(1)\right](\boldsymbol{\omega}^F\times\mathbf{n}_{pq}).\end{aligned} \tag{A.1}$$

The superscripts t and r denote translation and rotation. $\mathbf{U}_t = \mathbf{U}_{pq} - (\mathbf{U}_{pq}\cdot\mathbf{n}_{pq})\mathbf{n}_{pq}$ and $\boldsymbol{\omega}^F = \boldsymbol{\omega}_{pq}+4\alpha^{-1}\boldsymbol{\omega}_p+4\alpha\boldsymbol{\omega}_q$ (where $\boldsymbol{\omega}_{pq} = \boldsymbol{\omega}_p+\boldsymbol{\omega}_q$) are the tangential translational and rotational speeds. h_o^t, and h_o^r are the translational and rotational lubrication cutoffs below which the corrections are applied. Similarly, the lubrication torques due to translation and rotation are given by

$$\begin{aligned}\mathbf{T}_p^{t,lub} &= 8\pi\mu R_{hyd}^2\left[\frac{\alpha(4+\alpha)}{10(1+\alpha)^2}\ln\left(\frac{h}{h_o^t}\right)+O(1)\right](\mathbf{n}_{pq}\times\mathbf{U}_{pq})\\ \mathbf{T}_p^{r,lub} &= 8\pi\mu R_{hyd}^3\left[\frac{2\alpha}{5(1+\alpha)}\ln\left(\frac{h}{h_o^r}\right)+O(1)\right]\boldsymbol{\omega}^T\end{aligned} \tag{A.2}$$

where $\boldsymbol{\omega}^T = \left(\boldsymbol{\omega}_p + \frac{\alpha\boldsymbol{\omega}_q}{4}\right) - \left[\left(\boldsymbol{\omega}_p + \frac{\alpha\boldsymbol{\omega}_q}{4}\right) \cdot \mathbf{n}_{pq}\right] \mathbf{n}_{pq}$. The equations above (Eqs. A.1 and A.2) include the $O(1)$ terms. Since the analytical results are valid in the limit of small interparticle gaps, we estimated these term from the values given by O'Neill and Majumdar (1970) for $h/R = 0.001$. The lubrication forces (normal and tangential) and torques on the q^{th} particle can be written as $\mathbf{F}_q = -\mathbf{F}_p$ and $\mathbf{T}_q = \mathbf{T}_p$. By taking the limit $\alpha \to \infty$ in Eqs. 1, A.1, and A.2 and replacing q with w to denote a wall, one can derive the equations for the lubrication correction on a particle near a wall. These wall contributions are added with the particle-particle lubrication correction to obtain the total forces and torques. From benchmark simulations of steady translation and rotation of rigid particles at varying gaps, the tangential lubrication cutoffs are estimated to be $h_o^t/R_{hyd} = h_o^r/R_{hyd} = 0.1$ and $h_o^{w,t}/R_{hyd} = h_o^{w,r}/R_{hyd} = 0.1$ (where $h_o^{w,t}$ and $h_o^{w,r}$ are the particle-wall lubrication cutoffs). The forces and torques computed by LBM saturate to a constant value for gap sizes smaller than these thresholds.

REFERENCES

Bergenholtz, J., Brady, J. F. and Vicic, M. (2002) The non-Newtonian rheology of dilute colloidal suspensions. *Journal of Fluid Mechanics*, **456**, 239–275.

Bird, R. B., Stewart, W. E. and Lightfoot, E. N. (2007) *Transport phenomena*. John Wiley & Sons.

Blanc, F., Peters, F. and Lemaire, E. (2011) Local transient rheological behavior of concentrated suspensions. *Journal of Rheology*, **55**, 835–854.

Brady, J. F. and Bossis, G. (1985) The rheology of concentrated suspensions of spheres in simple shear flow by numerical simulation. *Journal of Fluid Mechanics*, **155**, 105–129.

Brown, E. and Jaeger, H. M. (2014) Shear thickening in concentrated suspensions: phenomenology, mechanisms and relations to jamming. *Reports on Progress in Physics*, **77**, 046602.

Chen, S. and Doolen, G. D. (1998) Lattice Boltzmann method for fluid flows. *Annual Review of Fluid Mechanics*, **30**, 329–364.

Dbouk, T., Lobry, L. and Lemaire, E. (2013) Normal stresses in concentrated non-Brownian suspensions. *Journal of Fluid Mechanics*, **715**, 239–272.

Fall, A., Lemaitre, A., Bertrand, F., Bonn, D. and Ovarlez, G. (2010) Shear thickening and migration in granular suspensions. *Physical Review Letters*, **105**, 268303.

Feng, Z. G. and Michaelides, E. E. (2004) The immersed boundary-lattice Boltzmann method for solving fluid-particles interaction problems. *Journal of Computational Physics*, **195**, 602–628.

Gadala-Maria, F. and Acrivos, A. (1980) Shear-induced structure in a concentrated suspension of solid spheres. *Journal of Rheology*, **24**, 799–814.

Guazzelli, E. (2017) Rheology of dense suspensions of non colloidal particles. In *EPJ Web of Conferences*, vol. 140, 01001. EDP Sciences.

Jogun, S. and Zukoski, C. F. (1996) Rheology of dense suspensions of plate-like particles. *Journal of Rheology*, **40**, 1211–1232.

Kolli, V. G., Pollauf, E. J. and Gadala-Maria, F. (2002) Transient normal stress response in a concentrated suspension of spherical particles. *Journal of Rheology*, **46**, 321–334.

Krieger, I. M. and Dougherty, T. J. (1959) A mechanism for non-Newtonian flow in suspensions of rigid spheres. *Transactions of the Society of Rheology*, **3**, 137–152.

Kulkarni, P. M. and Morris, J. F. (2008) Suspension properties at finite Reynolds number from simulated shear flow. *Physics of Fluids*, **20**, 040602.

Lorenz, E., Sivadasan, V., Bonn, D. and Hoekstra, A. G. (2018) Combined lattice-Boltzmann and rigid-body method for simulations of shear-thickening dense suspensions of hard particles. *Computers & Fluids*, **172**, 474–482.

Nguyen, N. Q. and Ladd, A. J. C. (2002) Lubrication corrections for lattice-Boltzmann simulations of particle suspensions. *Physical Review E*, **66**, 046708.

O'Neill, M. E. and Majumdar, R. (1970) Asymmetrical slow viscous fluid motions caused by the translation or rotation of two spheres. Part 1. The determination of exact solutions for any values of the ratio of radii and separation parameters. *Zeitschrift für angewandte Mathematik und Physik ZAMP*, **21**, 164–179.

Peters, F., Ghigliotti, G., Gallier, S., Blanc, F., Lemaire, E. and Lobry, L. (2016) Rheology of non-Brownian suspensions of rough frictional particles under shear reversal: A numerical study. *Journal of Rheology*, **60**, 715–732.

Shan, X. and Chen, H. (1993) Lattice Boltzmann model for simulating flows with multiple phases and components. *Physical Review E*, **47**, 1815.

Simeonov, J. A. and Calantoni, J. (2012) Modeling mechanical contact and lubrication in direct numerical simulations of colliding particles. *International Journal of Multiphase Flow*, **46**, 38–53.

Simon, D. B., Hormozi, S., Guazzelli, E. and Pouliquen, O. (2015) Rheology of dense suspensions of non-colloidal spheres in yield-stress fluids. *Journal of Fluid Mechanics*, **776**.

Srinivasan, S., Van den Akker, H. E. A. and Shardt, O. (2020) Shear thickening and history-dependent rheology of monodisperse suspensions with finite inertia via an immersed boundary lattice Boltzmann method. *International Journal of Multiphase Flow*, 103205.

Stickel, J. J. and Powell, R. L. (2005) Fluid mechanics and rheology of dense suspensions. *Annual Review of Fluid Mechanics*, **37**, 129–149.

Ten Cate, A., Derksen, J. J., Portela, L. M. and Van den Akker, H. E. A. (2004) Fully resolved simulations of colliding monodisperse spheres in forced isotropic turbulence. *Journal of Fluid Mechanics*, **519**, 233–271.

Thorimbert, Y., Marson, F., Parmigiani, A., Chopard, B. and Lätt, J. (2018) Lattice Boltzmann simulation of dense rigid spherical particle suspensions using immersed boundary method. *Computers & Fluids*, **166**, 286–294.